



Cite this: DOI: 10.1039/d6ey00083e

## Low hydrogen crossover anion-exchange membrane water electrolysis based on non-ionic binder polymers

 Oscar Strobl,<sup>a</sup> Nemanja Martić,<sup>a</sup> Hannes Michaels,<sup>a</sup> Felipe Not de Godoy,<sup>a</sup> Franka Wessnick,<sup>a</sup> Daniel Lang,<sup>a</sup> Michael Kress,<sup>a</sup> Anna Maltenberger,<sup>a</sup> Sönke Wengler-Rust,<sup>b</sup> Thomas Luxbacher,<sup>c</sup> Steffen Falgner,<sup>b</sup> Patrick Borowski,<sup>d</sup> Artjom Maljusich,<sup>d</sup> Andre Klinger and Günter Schmid

The quest for high energy efficiencies pushes anion-exchange membrane water electrolysis (AEMWE) to adopt designs comprising highly-functionalised ionomers. Unfortunately, undesirably high hydrogen crossover owing to such ionomer-based electrodes has so far gone unnoticed. Here, we report on AEMWE cells employing non-ionic fluorine-free binder polymers. The hydrophobic electrodes expel liquid electrolyte from transport pathways, thereby reducing hydrogen supersaturation pressures. As a result, hydrogen crossover is multifold reduced (down to 0.8% at 2 A cm<sup>-2</sup>). Strikingly, even the electrolyser overpotential is reduced by 40 mV compared to an anion-exchange ionomer owing to facile gas transport, affording electrolyser loads of 1.5 A cm<sup>-2</sup> at 1.88 V at 60 °C. The non-ionic cathodes show durability beyond 1000 hours and operate in dual-feed as well as in dry-cathode mode. The introduced design allows to select electrode materials from much greater libraries, with the anticipated result of new generations of durable electrodes for water electrolysis and beyond.

 Received 23rd April 2026,  
Accepted 24th April 2026

DOI: 10.1039/d6ey00083e

[rsc.li/eescatalysis](https://rsc.li/eescatalysis)

### Broader context

Anion-exchange membrane water electrolysis (AEMWE) is widely regarded as a promising route toward low-cost and sustainable hydrogen production, enabling the use of earth-abundant catalysts under chemically mild and electrically dynamic operating conditions. Towards industrial implementation, however, electrolyser safety is of critical importance, in particular regarding H<sub>2</sub>/O<sub>2</sub> mixing due to hydrogen crossover. In the pursuit of high cell efficiencies, AEMWE electrode designs have oftentimes adopted architectures similar to proton-exchange membrane electrolysis, incorporating catalyst layers comprising functionalised ionomer binders. While these designs have demonstrated promising electrochemical performance, systematic investigations of hydrogen crossover remain scarce, limiting the establishment of clear links between electrode materials, gas transport, and operational safety. This work elucidates how such ionomer-rich cathode layers unfortunately suffer from excessive electrode flooding, leading to gas-transport limitations and ultimately to critically high hydrogen crossover. In contrast, substituting functionalised ionomers with non-functionalised binder polymers yields catalyst layers with increased hydrophobicity, resulting in markedly reduced hydrogen crossover without compromising electrolyser efficiency. The mechanistic description in this paper links electrode wetting, gas transport and hydrogen crossover into a key design criterion for AEMWE electrodes. In turn, our findings establish general design guidelines towards electrode fabrication for safer and industrially viable AEMWE operation.

Anion-exchange membrane (AEM) water electrolysis (AEMWE) offers dynamic hydrogen production at high current densities and

high gas purities using low-cost materials.<sup>1,2</sup> Active catalysts<sup>3,4</sup> and growing understanding of failure mechanisms<sup>5,6</sup> have pushed AEM electrolysis to power densities, energy efficiencies and durability approaching those of established alkaline and proton-exchange-membrane electrolysis.<sup>7-11</sup>

As the quest for ever-higher energy efficiencies drives electrolyser designs towards thin membranes, hydrogen gas crossover effects arise and must not be disregarded. Large supersaturation pressure leads to undesired hydrogen gas

<sup>a</sup> Siemens Energy Global GmbH and Co. KG, Schuckertstrasse 2, 91058 Erlangen, Germany. E-mail: hannes.michaels@siemens-energy.com

<sup>b</sup> Anton Paar Germany GmbH, Hellmuth-Hirth-Strasse 6, 73760 Ostfildern, Germany

<sup>c</sup> Anton Paar GmbH, Anton-Paar-Strasse 20, 8054 Graz, Austria

<sup>d</sup> Evonik Operations GmbH, Research, Development & Innovation, Paul-Baumann-Strasse 1, 45772 Marl, Germany

† These authors contributed equally.



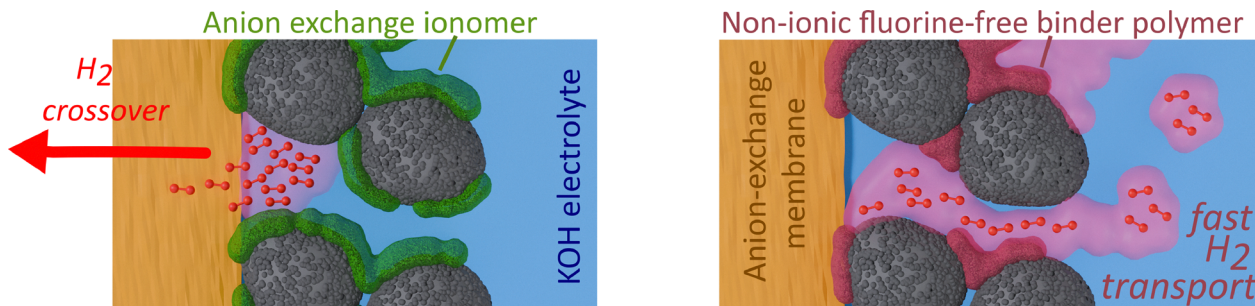


Fig. 1 Hydrogen crossover in anion-exchange membrane electrolyzers is mitigated with direct-membrane-coated electrodes based on non-ionic, fluorine-free binder polymers.

crossover into the anode oxygen gas stream if produced hydrogen gas is not transported out of the cathode catalyst layer sufficiently fast. This poses the risk of explosive  $H_2/O_2$  mixtures, particularly at low current densities.<sup>12,13</sup>

Supersaturation pressure in the catalyst layer due to accumulation of produced hydrogen gas is caused by too narrow or blocked transport channels in the catalyst structure.<sup>14</sup> In many cases, this is caused by excessive liquid electrolyte in the pores of the catalyst layers (Fig. 1a); such *electrode flooding* was extensively studied for *e.g.* hydrogen fuel cells or  $CO_2$  electrolysis electrodes.<sup>15–17</sup>

In most reports on AEMWE, electrode design rules are adapted from proton-exchange-membrane water electrolyzers (PEMWE): Catalyst layers comprise highly-functionalised ionomers, despite operating the cells in alkaline supporting electrolyte. In PEMWE (usually operated in ultra-pure water), the amphiphilic poly(perfluoro sulfonic acid) polymers (PFSA) form ionic channels required for proton transport, but repel excessive water from the catalyst layer.<sup>18,19</sup> In contrast, most anion-exchange ionomers are based on fluorine-free polymers, which do not repel water to the degree of PFSA.<sup>20,21</sup> As a result, AEMWE catalyst layers lack hydrophobic sites, associated with bubble nucleation and gas transport paths.<sup>22,23</sup>

While  $H_2$  crossover data remains frequently unreported in AEMWE literature to date, first very recent contributions observed greatly elevated undesired  $H_2$  crossover levels (>4%) at partial load.<sup>13</sup> Elsewhere, gas transport was shown to be improved in AEMWE/alkaline electrolyser cells by *e.g.* implementing poly(tetra-fluoroethylene) (PTFE) into gas-diffusion-type electrode structures.<sup>24–26</sup> Nonetheless, all perfluorinated materials are currently under assessment for their lasting environmental impact due to bioaccumulation, and alternative solutions need be explored urgently.<sup>27</sup>

Here, we report fluorine-free catalyst layers based on non-ionic binder polymers that afford AEMWE with low hydrogen crossover (Fig. 1b). The cathode catalyst layers with strong adhesion are prepared by direct-membrane coating. We demonstrate how in the presence of mild alkaline electrolyte, ionic functionalisation of the catalyst layer binder polymer is not required for ionic transport in the catalyst layer, not even in dry-cathode operation. The non-ionic polymer affords hydrophobic, yet fluorine-free electrodes. The consequence is a multifold

reduction in hydrogen gas crossover at all current densities (0.8% at  $2\text{ A cm}^{-2}$  and <2% down to  $0.25\text{ A cm}^{-2}$ , compared to 2% at  $2\text{ A cm}^{-2}$  for electrodes based on a strongly hydrophilic anion-exchange ionomer). Further, facile hydrogen transport out of the catalyst layer affords a 40 mV reduced overpotential at  $2\text{ A cm}^{-2}$ . The introduced design strategies open new pathways to scalable, durable and sustainable electrodes for water electrolysis.

## Results and discussion

We propose catalyst layers based on non-ionic binder polymers, which afford a number of advantages over the traditional design employing anion-exchange ionomers. Generally, requirements such as chemical, mechanical and thermal durability need to be met by any material in the electrolyser cell. In contrast, it is demonstrated in ensuing sections that ionic conductivity is not required for the cathode binder polymer in the presence of mild supporting electrolyte. The exemplary commercial example materials chosen in this study are the poly(imidazolium)-based anion-exchange ionomer AP3-HNN9, and the non-ionic polymer poly(vinyl benzyl chloride) (PVBC). The binder polymers were utilised to cast cathode catalyst layers by direct-membrane coating onto a  $\approx 75\text{ }\mu\text{m}$  thick reinforced DURAION AEM provided by Evonik, as described in ensuing sections.

### Electrolyser operation

Direct-membrane-coated cathodes (to be described below) were examined in  $25\text{ cm}^2$  single-cell AEM-electrolyser tests in dual-feed configuration, *i.e.*, feeding electrolyte into both anode and cathode. The  $25\text{ cm}^2$  testing was carried out in a designated test cell published *via* the AEMDirekt consortium;<sup>28</sup> the cell drawings are available from the authors upon reasonable request. The electrodes were benchmarked in two cell configurations: (1) the base cell design of AEMDirekt, where the cathode is contacted by a plain 316L Siemens-energy-internal porous transport layer, in order to be able to attribute all observations specifically regarding hydrogen crossover to the catalyst layers themselves (rather than masking any trends by the use of gas-diffusion-type electrodes); and (2) a performance-improved cell design where a Siemens-energy-internal carbon fleece is



inserted between the cathode catalyst layer and the stainless steel porous transport layer. In both configurations, the same plain stainless steel porous transport layer is used as anode transport layer and catalyst at once (similar to previous literature<sup>29</sup>).

The electrochemical performance of the cathode catalyst layers based on the two binder polymer configurations is initially evaluated in the first cell configuration (Fig. 2a). In this base configuration, the electrolyser operated at 2.24 V at 2 A cm<sup>-2</sup> for the electrode based on the anion-exchange ionomer and 2.20 V for the non-ionic polymer, respectively. The cell potentials of the cathode based on the hydrophobic PVBC are 40 mV improved towards lower cell voltages compared to the anion-exchange ionomer. This demonstrates that the proposed electrode design is without drawbacks equally applicable under practical AEMWE conditions. It is evident that additional ionomer-based ionic transport through the polymer in the catalyst layer is not required in presence of mild alkaline supporting electrolyte. Notably, no increases in the overpotential slopes at high current densities are observed, indicating that the cathode catalyst layer is not under-supplied of reactant water in these conditions. Rather, a small improvement in cell potentials at high current densities appears to stem from reduced mass transport resistance to propel product gas away from the catalyst sites.

In consequence, the reliable operation of the AEM electrolyser cells based on non-ionic polymers is demonstrated through stable operation in a constant-current hold at 1.5 A cm<sup>-2</sup> for >1000 h in combination with a Siemens Energy carbon felt contacting the cathode (Fig. S3). The electrolyser cell based on the non-ionic polymer showed a begin-of-life voltage of 1.88 V and operated for >1000 h with around 90 μV h<sup>-1</sup> degradation. These test results indicate suitability of the proposed robust electrode designs to be scaled to pressurised kW-MW stacks. Further improvements in the cell voltages will be achieved by combining the here-presented cathodes with a highly active anode catalyst, selecting optimal contact structures for anode and cathode, and increasing the operating temperature of the electrolyser.

For purposes of improved hydrogen gas purity and reduced balance-of-stack periphery, it has been demonstrated to be beneficial to operate AEM electrolysers in dry-cathode, *e.g.* not feeding any supporting electrolyte into the cathode compartment.<sup>30,31</sup> In this configuration, if no supporting electrolyte is present in the cathode, it would seem ionic functionalisation of the polymer would be required to maintain sufficient hydration, readily at moderate current densities around 1.5 A cm<sup>-2</sup>.<sup>32,33</sup> Strikingly, the presented cathodes based on the non-ionic hydrophobic polymer (for comparative purposes in the first electrode

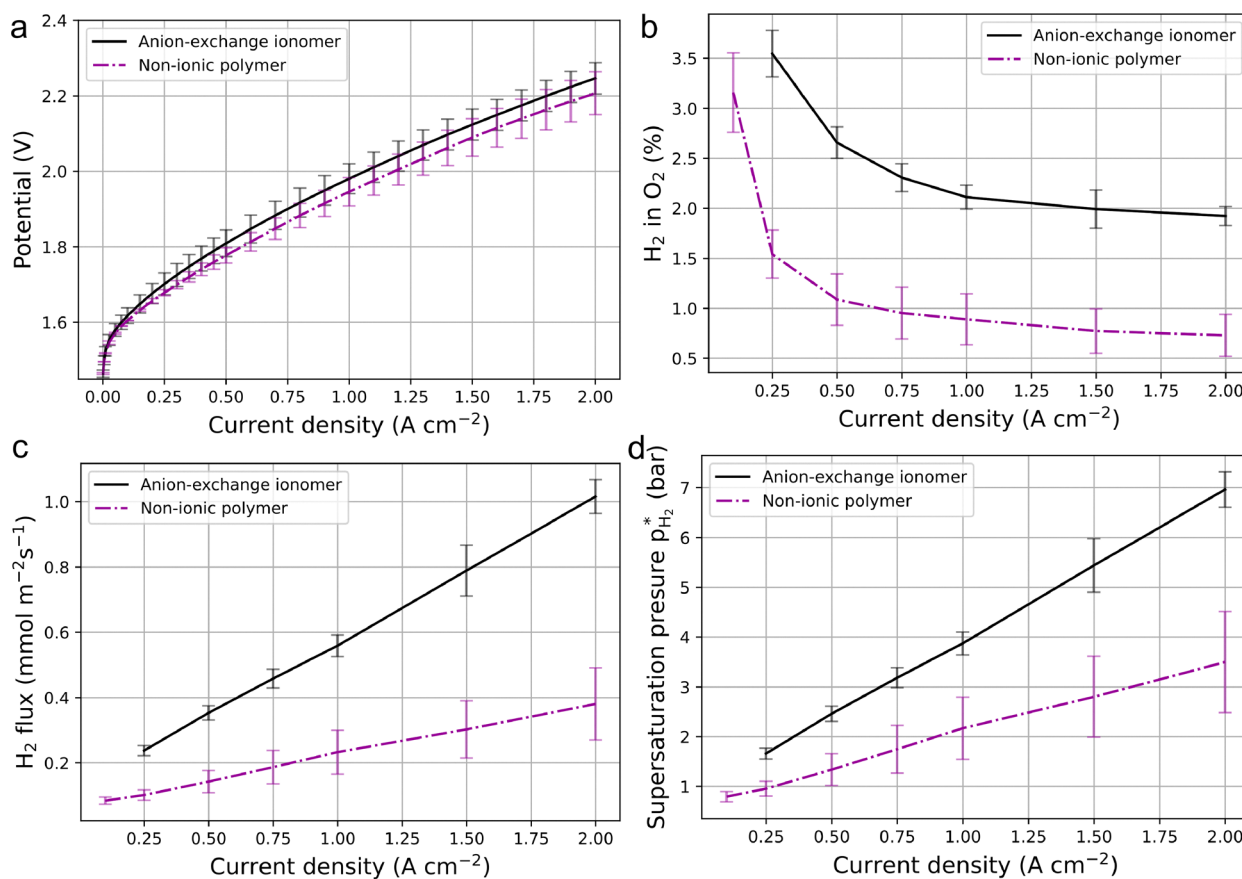


Fig. 2 (a) Polarisation curves, (b) hydrogen crossover and (c) molar hydrogen flux versus applied current density during a staircase profile for anion-exchange-membrane water electrolyser cells comprising cathode catalyst layers based on either an anion-exchange ionomer or a non-ionic hydrophobic polymer; (d) calculated hydrogen supersaturation pressure at the cathode; all experiments carried out at 60 °C ambient pressure.



configuration without any gas diffusion layer) operate reliably even in dry-cathode operation without any signs of mass transport limitations up to  $2 \text{ A cm}^{-2}$  (Fig. S4a). It appears that small amounts of KOH salt pass, which through the membrane from anode to cathode due to swelling of the membrane, create sufficient driving force for water supply: a salt gradient builds up, which alone affords the required water transport. This mechanism appears to be in sufficient effect irrespective of the cathode binder polarity. As the electrolysis consumes water on the cathode, the local concentration of KOH increases. In turn, a gradient in osmotic pressure generated by the gradient in salt concentration *versus* the anode. Provided the required water flux from anode to cathode for faradaic water electrolysis consumption at  $2 \text{ A cm}^{-2}$  of  $3.7 \times 10^{-3} \text{ L m}^{-2} \text{ s}^{-1}$ , assuming common AEM water permeabilities<sup>34</sup> of  $A_{\text{H}_2\text{O}} \approx 10^{-5} \text{ L m}^{-2} \text{ s}^{-1} \text{ bar}^{-1}$ , the osmotic gradient pressure gradient  $\Delta\pi = \frac{J_{\text{H}_2\text{O}}}{A_{\text{H}_2\text{O}}}$  is estimated around  $\geq 100 \text{ bar}$ ; in turn, the expected concentration gradient (in a first approximation disregarding activity coefficients/...)  $\Delta c = \frac{\pi}{nRT}$  with  $n = 2$  for KOH is estimated around  $\geq 2 \text{ bar}$ , *i.e.* with  $1 \text{ M}$  KOH in the anode, at least  $3 \text{ M}$  local concentration is expected at the dry cathode. Given the magnitude of this estimated osmotic pressure, this transport mechanism and therefore electrode concept is expected to hold even against *e.g.*  $10\text{--}30 \text{ bar}$  differential pressure.

In a constant-current hold at a current density of  $1.5 \text{ A cm}^{-2}$ , a further two-fold reduction in the  $\text{H}_2$  crossover down to  $\approx 0.3\%$  is observed in dry-cathode compared to dual-feed operation. The feasibility of the proposed non-ionic design is confirmed, even in dry-cathode operation. Electrolyser cell voltages are expected to improve significantly when the presented material concepts will be implemented into cell configurations featuring highly active anode catalysts and optimal contact structures for anode and cathode.

### Hydrogen crossover

The hydrogen crossover as function of applied current density of the two electrode configurations was recorded in a downwards-staircase profile from  $2 \text{ A cm}^{-2}$  towards  $0.1 \text{ A cm}^{-2}$  at  $60 \text{ }^\circ\text{C}$  and ambient pressure (Fig. 2b and Table 1). At each current density, sufficient time was afforded for the  $\text{H}_2$  crossover reading to stabilise (Fig. S5).

The hydrogen crossover for the cells based on the traditional anion-exchange ionomer was around  $2\%$  at  $2 \text{ A cm}^{-2}$  and

increased to  $3.5\%$  at  $0.25 \text{ A cm}^{-2}$ . Given that a safety threshold of  $2\% \text{ H}_2$  in  $\text{O}_2$  is mandatory for large electrolyser plants, this implies that electrolyser cells based on many proposed designs in literature comprising electrodes based on anion-exchange ionomers would practically not be scalable to operate in industrial settings. Therefore, such hydrogen crossover and hence underlying hydrogen supersaturation pressure needs to be mitigated. In consequence, the fluorine-free non-ionic and therefore hydrophobic binder polymer poly(vinyl benzyl chloride) was introduced to replace anion-exchange ionomer as binder polymer in the cathode catalyst layer. The resulting catalyst layers were found to be significantly hydrophobic with water/air contact angles of around  $130^\circ$  (compared to  $68^\circ$  for ionomer-based electrodes, see below in Fig. 4b and c). Indeed, the resulting hydrogen crossover is reduced across all current densities, showing  $\approx 3\%$  at current densities as low as  $0.1 \text{ A cm}^{-2}$  down to  $0.72\%$  at  $2 \text{ A cm}^{-2}$ . Therefore, through the implementation of non-ionic fluorine-free binder polymers, safe electrolyser operation down to  $\approx 20\%$  of the nominal current density is achieved. In this sense, the present results mirror earlier reports on dry-cathode operation, where low hydrogen crossover values were observed; here, comparable behaviour is observed through deliberate tuning of the cathode wettability *via* the selection of a hydrophobic binder polymer.

Eqn (S8) is applied to convert the hydrogen crossover sensor readings  $Y_{\text{H}_2}$  (in%) to a molar flux of hydrogen into the anode per unit area and time ( $J_{\text{exp}}$ , Fig. 2c). The hydrogen flux increases linearly with current-density in both electrode configurations. The slopes of the two lines converging onto a similar y-offset confirms that the reduced hydrogen crossover indeed stems from electrode transport and not membrane effects.<sup>14</sup>

Subsequently, a physicochemical transport model is applied to the obtained data to model hydrogen generation in the cathode catalyst layer. The underlying mathematical description of a transport velocity of hydrogen gas out of the cathode catalyst layer was adapted from earlier efforts from our group;<sup>35</sup> the description for the presented case is derived in the SI. The model includes faradaic hydrogen generation at the cathode, transport through the cathode catalyst layer into the electrolyte bulk, as well as hydrogen crossover towards the anode by means of diffusion and electroosmotic drag. The drag coefficient of the membrane was estimated by evaluating the electrolyte fill level readings during each current density step of the staircase profile (Fig. S6), giving a drag coefficient  $\xi$  around  $1.5 \text{ H}_2\text{O}$  per  $\text{OH}^-$  (Fig. S7).

Table 1 Experiment data and model results by cathode configuration

		Anion-exchange ionomer	Hydrophobic polymer
Experiment data	$\text{H}_2$ in $\text{O}_2$ @ $2 \text{ A cm}^{-2}$ (%)	$1.9 \pm 0.1$	$0.72 \pm 0.2$
	$\text{H}_2$ in $\text{O}_2$ @ $0.1 \text{ A cm}^{-2}$ (%)	$> 4$	$3.1 \pm 0.3$
Model results	$p_{\text{H}_2}^*$ @ $2 \text{ A cm}^{-2}$ (bar)	$7.0 \pm 0.3$	$3.5 \pm 0.7$
	$k_1$ ( $\text{mm s}^{-1}$ )	$34 \pm 4$	$97 \pm 30$
	$D_{\text{H}_2}^{\text{diff}}$ ( $10^{-8} \text{ m}^2 \text{ s}^{-1}$ )	$2.7 \pm 0.3$	$2.0 \pm 0.4$
	Transport time (ms)	$0.29 \pm 0.3$	$0.1 \pm 0.3$



The central obtained parameter from the physicochemical model is the supersaturation pressure at the boundary layer between cathode and membrane  $p_{\text{H}_2}^*$  (Fig. 2d). Large supersaturation pressure not only increases the gradient of hydrogen pressure across the membrane provoking diffusion towards the anode, but also increases mechanical forces within the cathode catalyst layer, potentially resulting in faster deterioration of the catalyst layer. This supersaturation pressure increases with increasing current density as more product gas is accumulating in the cathode catalyst layer. In case of the anion-exchange ionomer, the transport of hydrogen gas out of the cathode into the bulk is blocked by liquid electrolyte penetrating into the catalyst layer pores. In consequence, the supersaturation pressure is estimated to reach around 7 bar at  $2 \text{ A cm}^{-2}$ . In case of the hydrophobic polymer, the pressure at the boundary layer is two-fold lower around 3.5 bar, indicating facile hydrogen transport out of the cathode layer.

The transport rate of hydrogen out of the cathode is represented in the mathematical model as a transport coefficient  $k_1$  (in  $[\text{m s}^{-1}]$  and therefore comparable to a velocity). In accordance with the decrease in cathode supersaturation pressure, the transport velocities are estimated as  $34 \text{ mm s}^{-1}$  in the electrode based on the anion-exchange ionomer, and  $97 \text{ mm s}^{-1}$  in the electrode based on the hydrophobic hydrocarbon polymer (Tab. 1). For the effective diffusion coefficient through the swollen membrane, similar values for both electrode configurations are obtained from the mathematical model, around  $2.7 \pm 0.3 \times 10^{-8} \text{ m}^2 \text{ s}^{-1}$  and  $2.0 \pm 0.4 \times 10^{-8} \text{ m}^2 \text{ s}^{-1}$ , respectively. This provides initial confirmation that the underlying transport processes are accurately attributed in the model: Hydrogen crossover is reduced in case of the hydrophobic polymer, as hydrogen transport out of the cathode occurs faster, while the effective membrane coefficient, independent of possible electrode configurations, remains unchanged. Applying the obtained effective transport velocities across the catalyst layer thickness of  $\approx 10 \mu\text{m}$  gives effective transport times for hydrogen out of the cathode of 0.29 ms for the anion-exchange ionomer, while only 0.10 ms for the cathodes based on the hydrophobic polymer.

The reduced hydrogen crossover is directly linked to the contact angle of the electrodes *via* a Young-Laplace description: A hydrophobic contact angle leads to de-wetted catalyst layer pores readily at lower capillary pressures. As a consequence, the liquid saturation of the catalyst layer pores is reduced. In turn, the pore network in the catalyst layer remains gas-connected and hydrogen transport occurs more rapidly. The reader is referred to the detailed derivation in the SI regarding the extraction of related transport parameters, such as catalyst layer liquid saturation and effective hydrogen diffusion coefficients.

Once a set of material parameters is obtained, our model allows the estimation of how modifications in the cell components affect macroscopic parameters such as hydrogen crossover. For instance, at small current densities where the effect of drag is small ( $J_{\text{H}_2}^{\text{drag}} \ll J_{\text{H}_2}^{\text{diff}}$ ), the observed hydrogen crossover scales inversely with the membrane thickness  $Y_{\text{H}_2} \propto J_{\text{exp}} \propto \frac{D_{\text{eff}}}{\delta_{\text{m}}}$ . Assuming membrane materials with similar

$D_{\text{eff}}$ , Fig. S8 shows how the hydrogen crossover is expected to decrease with effective wet membrane thickness. Based on the ionomer-based electrode design, membrane thicknesses of  $> 150 \mu\text{m}$  would be required to reduce the hydrogen crossover down to  $< 2\%$ . However, for such thick membranes, area-specific resistances of  $\geq 250 \text{ m}\Omega \text{ cm}^2$  are expected, which would lead to electrolyser voltages far beyond economic viability. For deeper analyses of the leverages of *e.g.* electrode gas transport velocities on the hydrogen crossover, the reader is referred to our earlier publication.<sup>35</sup> Overall, this estimation is a clear signal that strategies to reduce hydrogen crossover must be sought in both membrane and electrodes.

### Direct-membrane-coating

When scaling electrolyser technologies to industrial production, spray coating highly-volatile alcohol-based catalyst inks, as employed in many reports on high-performing AEMWE, is not feasible due to safety concerns regarding the large amounts of evaporating volatile flammable solvents.<sup>36</sup> In contrast, direct-membrane coating offers low-waste, high-precision deposition of firmly-adhering electrodes.<sup>37,38</sup> Industrial-scale coating processes commonly employ high-boiling solvents to control evaporation kinetics during drying steps.<sup>39–41</sup> However, compared to metal and metal-oxide substrates, most ion-exchange membranes for AEMWE or PEMWE are at risk of morphological and/or microstructural deterioration at temperatures above  $150 \text{ }^\circ\text{C}$ . This constrains drying steps to moderate temperatures and slows down drying processes. As a consequence, slower drying often leads to less-porous catalyst layers with narrow transport channels for product gases. Here, we show how AEMWE electrodes with low hydrogen crossover are manufactured by direct-membrane-coating based on non-ionic fluorine-free polymers.

First, catalyst pastes were prepared from stock solutions of the respective polymer and the platinum black catalyst. Fig. 3a shows the amplitude sweeps for pastes based on the anion-exchange ionomer and non-ionic binder polymers. The ionomer-based paste shows a pronounced network in form of a linear viscoelastic region. The non-ionic polymer binder paste does not show such, hinting towards better dispersed catalyst particles forming a less pronounced network. The flow point  $\tau_f$  mirrors this observation, showing a shear stress of 5 Pa for the non-ionic and 29 Pa for the ionomer binder (Table 2). An increase in the storage modulus is observed at high amplitude for the non-ionic binder polymer paste; similar observations in literature link this behaviour to particle jamming through the collision of particles in the measuring gap.<sup>42</sup>

Fig. 3b shows the flow curves for the electrode pastes. The ionomer-containing paste shows a ten-fold higher low-shear viscosity than the non-ionic counterpart, highlighting the more pronounced network between the components. Both electrode slurries display pronounced shear thinning, reaching  $\approx 1 \text{ Pa s}$  for the ionomer and  $\approx 0.2 \text{ Pa s}$  for the non-ionic binder at  $1000 \text{ s}^{-1}$ . Interestingly, at shear rates where the shear stress is similar to where the particle jamming in the amplitude sweep occurs, the flow curve of the non-ionic paste shows a slight plateau, potentially highlighting an increased flow resistance.



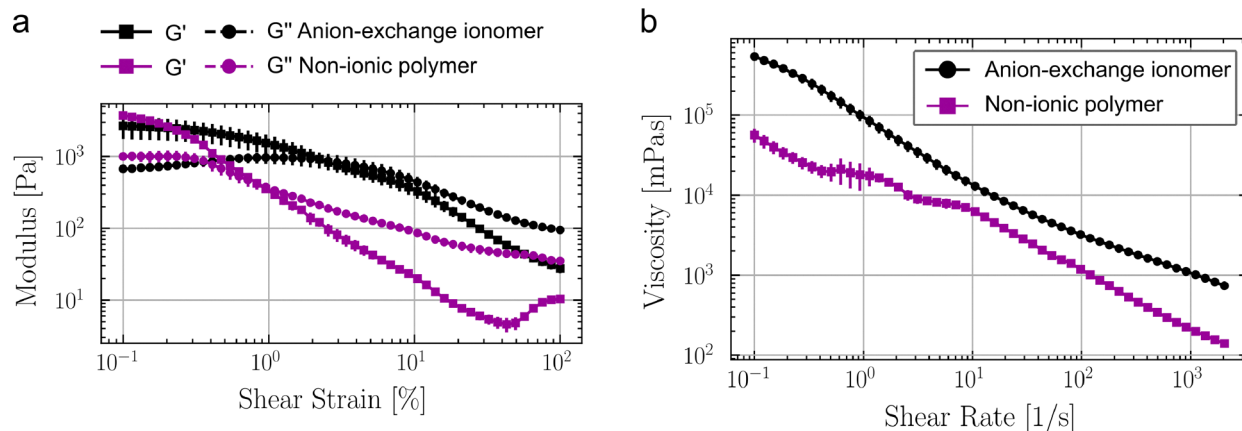


Fig. 3 (a) Rheological amplitude sweeps and (b) viscosity curves of electrode pastes.

Table 2 Key indicators of rheology and direct-membrane-coated electrodes

Paste parameter	Anion-exchange Ionomer	Non-ionic polymer
Yield stress $\tau_y$ (Pa)	$4.5 \pm 1.6$	—
Flow point $\tau_f$ (Pa)	$29 \pm 9$	$5.0 \pm 1.0$
Consistency index $K$ (Pa s)	$95 \pm 20$	$17.8 \pm 1.3$
Flow index $n$	$0.30 \pm 0.03$	$0.39 \pm 0.02$
Electrode parameter		
Contact angle $\theta$ (°)	$67.7 \pm 1.4$	$129.0 \pm 1.1$

The electrode slurries were applied by doctor-blade onto reinforced DURAION AEM provided by Evonik to obtain macroscopically homogeneous electrode layers (Fig. 4a). Consequently, we introduced the water/air contact angles of the different electrodes as measures of the wettability of the catalyst/polymer surface (Fig. 4b and c): The hydrophilic anion-exchange ionomer in combination with the Pt@C catalyst resulted in contact angles around  $\approx 68^\circ$ , while the hydrophobic polymer in combination with the catalyst formed a hydrophobic layer resulting in a contact

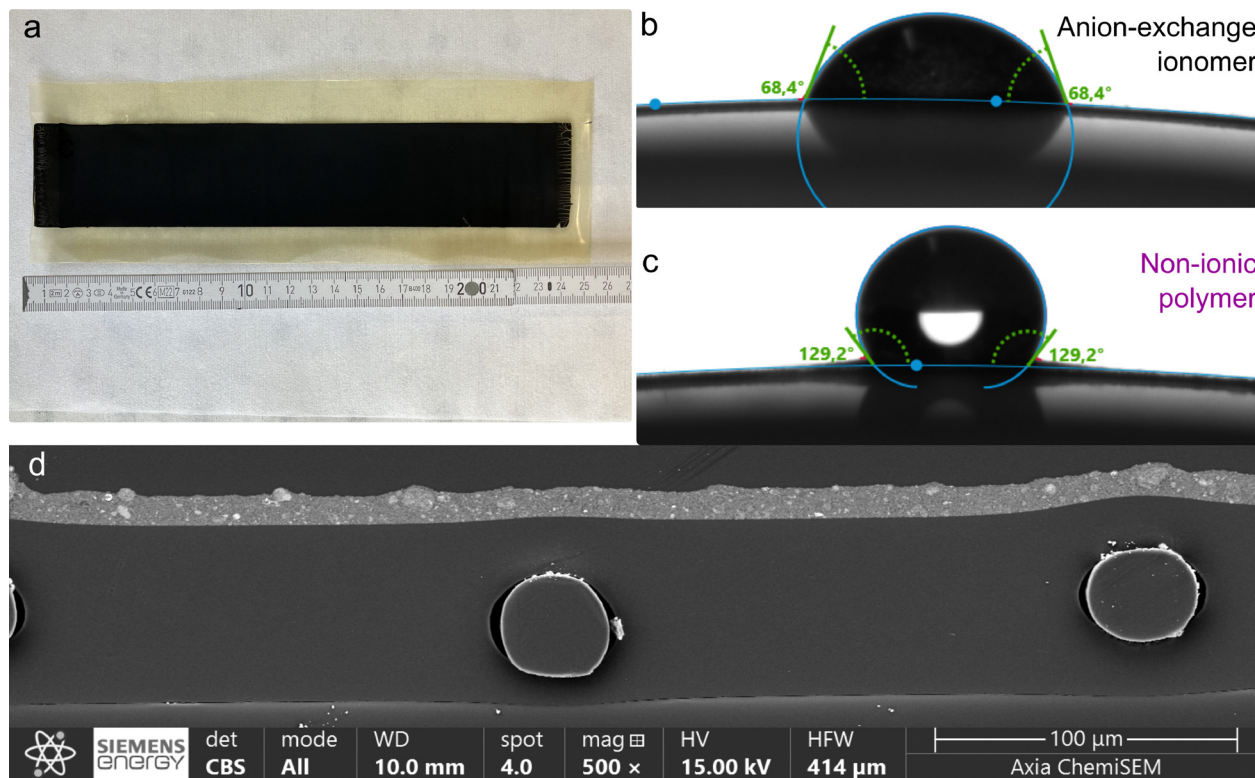


Fig. 4 (a) Photograph of cathode catalyst layer applied onto the reinforced DURAION AEM provided by Evonik; (b) water/air contact angle of catalyst layer based on the anion-exchange ionomer and (c) hydrophobic polymer; (d) cross-section electron microscopy of direct-membrane-coated cathode catalyst layer.



angle of  $\approx 129^\circ$ . This confirms that selecting non-ionic polymers as electrode binder polymers affords hydrophobic, yet fluorine-free electrodes that enable electrolyser operation with low hydrogen crossover by expelling excessive liquid electrolyte from gas transport pathways out of the catalyst layer.

pH-dependent apparent zeta potential measurements confirm the greater hydrophobicity of the electrode containing the non-ionic polymer compared to the electrode comprising the anion-exchange ionomer. At neutral to basic pH, the hydrophobic polymer exhibits a plateau in the apparent zeta potential at significantly larger absolute values than the ionomer, implying a more hydrophobic surface for the electrode containing the non-ionic polymer binder paste (Fig. S9).<sup>43,44</sup> While water molecules are repelled from hydrophobic surfaces, the adsorption of hydroxide ions may be favored resulting in a more negative zeta potential at neutral pH.<sup>45</sup> The anion-exchange ionomer with its cationic groups leads to a shift of the isoelectric point to higher pH.

A cross-section of a coated AEM confirms the homogeneity of the applied coating (Fig. 4a). The  $\approx 75 \mu\text{m}$  thick reinforced DURAION membrane comprises distinct  $\approx 25 \mu\text{m}$  circular reinforcement fibers. The dry catalyst layer thickness is obtained around 8–10  $\mu\text{m}$  (after drying of the initially applied as 45  $\mu\text{m}$  wet film).

Physisorption measurements (Fig. S10) reveal that the membrane-coated catalyst layers exhibit specific surface areas are of the same order of magnitude,  $5.09 \pm 0.03 \text{ m}^2 \text{ g}^{-1}$  and  $3.48 \pm 0.01 \text{ m}^2 \text{ g}^{-1}$  for the anion-exchange ionomer and the non-ionic polymer, respectively (as a reference, the specific surface area of the bare membrane was  $0.1 \text{ m}^2 \text{ g}^{-1}$ ). The rise of the isotherms for large relative pressures indicates the presence of macropores ( $> 50 \text{ nm}$ , see Fig. S10a and b).<sup>46</sup> In an attempt to quantify the macroscopic pore structure, the catalyst pastes were deposited onto a carbon felt for through-plane porometry (Fig. S11). Capillary flow porometry reveals that both electrode systems comprised through-plane pores of similar sizes, with mean flow pore sizes of  $1.00 \pm 0.02 \mu\text{m}$  and  $1.10 \pm 0.04 \mu\text{m}$ , respectively; this indicates that in such geometry, the macroscopic pore structure is governed by the underlying carbon felt (mean flow pore sizes of  $1.25 \pm 0.10 \mu\text{m}$ ).

## Conclusion and outlook

Non-ionic fluorine-free binder polymers allow to scale AEMWE electrolysers to industrial manufacture and deployment. Direct-membrane-coating is successfully employed to manufacture durable cathode layers. The hydrophobicity of the non-ionic polymers reduces the hydrogen supersaturation due to blocked transport pathways in the catalyst layers and affords significant reductions in hydrogen gas crossover, as well as improved overpotentials. Despite not providing any ionic conductivity, the electrodes operate without transport limitations even in dry-cathode configuration at  $2 \text{ A cm}^{-2}$ .

The non-ionic binder polymers were introduced here for direct-membrane-coated electrodes, nonetheless, the authors

have observed similar trends towards greatly reduced hydrogen crossover for *e.g.* substrate-coated (CCS-type) electrodes. Generally, removing the constraint of ionic conductivity from the electrode polymers allows to select from a much wider range of materials. Therefore, this report paves the way for new durable and scalable electrode designs, not only for AEMWE but likewise for other electrolyser technologies and beyond.

## Materials

1 M potassium hydroxide solution was procured from CSC Jaekle Chemie. The  $\approx 75 \mu\text{m}$  thick reinforced DURAION AEM was provided by Evonik to Siemens Energy under the AEMDirekt consortium agreement. The poly(vinyl benzyl chloride) hydrophobic binder polymer ( $M_n \approx 55\,000$ ,  $M_w \approx 100\,000$ ) in this case study, as well as any catalyst paste solvents, were purchased from Sigma-Aldrich. The HNN9 ionomer was purchased from Ionomr Innovations. A Siemens Energy stainless steel (316L) porous transport layer is used as anode without any further plating. The cathode catalyst employed is a platinum black. Porofil was obtained from Anton Paar QuantaTec, potassium chloride was purchased from Sigma-Aldrich, hydrochloric acid (0.5 M) and potassium hydroxide solution (0.5 M) were acquired from Carl Roth, nitrogen gas (99.999%) was purchased from Widmann Gase GmbH, Krypton gas (99.99%) was procured from air liquide. A carbon felt was purchased from Freudenberg performance materials. Further experimental details may be shared upon reasonable direct request to the authors under appropriate confidentiality agreements.

## Electrode pastes and rheology

The catalyst pastes for direct-membrane coating were prepared by blending the Pt@C-based cathode catalyst with a polymer stock solution in the paste solvent system and mixing three times for 5 minutes at 3500 rpm in a speed mixer (Hausschild). Further experimental details may be shared upon reasonable direct request to the authors under appropriate confidentiality agreements. After processing, the rheology of the pastes was measured using a rotational rheometer (MCR 92, Anton Paar, Austria) equipped with a plate–plate geometry (diameter 50 mm). The measurement gap was set to 0.35 mm, and excess material was trimmed prior to testing. A Peltier temperature control system maintained the sample at  $20^\circ\text{C}$  throughout the measurements. To minimize evaporation, a solvent trap was applied. Before the main characterization, the samples underwent an initial pre-shear at  $5 \text{ s}^{-1}$  for 60 s and a temperature control stage to ensure structural homogenization. The main procedure was performed in two stages:

1. Amplitude sweep: conducted at a constant angular frequency of  $\omega = 10 \text{ rad s}^{-1}$ , with strain amplitude  $\gamma$  ranging from 0.1% to 100%, to determine the linear viscoelastic region (LVE).
2. Flow curve: the viscosity  $\eta$  was measured as a function of shear rate  $\dot{\gamma}$  from  $0.1 \text{ s}^{-1}$  to  $2000 \text{ s}^{-1}$ .

All measurements were replicated at least twice to ensure reproducibility. The flow curve was fitted using the power-law model to obtain the paste-specific parameters: consistency index ( $K$ ) and flow behaviour index ( $n$ ). The yield point ( $\tau_y$ )



and flow point ( $\tau_f$ ) were extracted from the amplitude sweep based on the crossover and deviation of the storage modulus  $G'$  and loss modulus  $G''$ . The limit of the linear viscoelastic region (LVE) was defined as a 5% deviation according to ISO 6721-10.

### Electrode fabrication by direct-membrane coating

The catalyst paste was applied as a  $\approx 25$  cm-long stripe directly onto the reinforced DURAION AEM provided by Evonik by a doctorblade process on a vacuum chuck (Coatmaster 510, Erichsen). The coating speed was  $15 \text{ mm s}^{-1}$  ( $0.9 \text{ m min}^{-1}$ ). The coating gap was  $45 \mu\text{m}$  (Model 288, Erichsen). The cathodes were dried at  $60 \text{ }^\circ\text{C}$  for 14 hours. The Pt loading was around  $0.3 \text{ mg cm}^{-2}$  (determined by X-ray fluorescence, FISCHER-SCOPE X-RAY XDV -SDD).

### Contact angle measurements

The contact angle measurements were carried out on a Drop Shape Analyser DSA25 (Krüss). The drop shape was tracked with a camera at 10 frames per second. The contact angles were recorded between 1–5 seconds after the drops of the target liquid were placed onto the electrodes (to allow the drop shape to settle into shape, but before significant volume uptake into membrane/electrodes would occur). At least three drops of each target liquid were measured for each electrode configuration at different locations. The authors attempted to characterise the electrodes' free surface energies by combining the water/air contact angles with the contact angle of other liquids (diiodomethane, formamide, ...). Unfortunately, such contact angles were too small ( $< 5^\circ$ ) to allow accurate determination.

### Electron microscopy

The electron microscopy images were collected on an Axia microscope (Thermo Fisher).

### Membrane swelling

The in-plane ( $x,y$ )-swelling of membranes was evaluated using an optical microscope (VHX 6000, Keyence). The membrane samples were cut into pieces measuring  $8 \text{ mm} \times 10 \text{ mm}$ . The samples were positioned between two glass slides and the precise dry dimensions were recorded using the integrated software of the microscope. Subsequently, the membrane samples were immersed in the target medium in an oven at the target temperature for 24 hours prior to repeating the measurement. A steel plate comprising an adjustable heating cartridge was positioned on the microscope to maintain the target temperature during the measurement. To prevent the sample from drying during analysis, several drops of the target solution were added between the glass slides.

Out-of-plane ( $z$ )-swelling was evaluated by recording the thickness of a series of membrane samples using a Mitutoyo micrometer gauge.

The reported swelling values at elevated temperatures should be regarded as best estimates, the authors are aware that rapid drying kinetics of the specimens, especially at elevated temperatures, may result in underestimation of the media uptakes.

The volumetric electrolyte uptake  $\varepsilon_m$  is calculated as the relative volume increase.

$$\varepsilon_m = \frac{V_{\text{wet}}(t, c_{\text{KOH}}) - V_{\text{dry}}(t)}{V_{\text{wet}}(t, c_{\text{KOH}})} \quad (1)$$

### Membrane permeability

The permeability of hydrogen of the dry membrane was quantified in a permeation cell comprising two compartments, separated by the membrane sample. Both chambers were initially evacuated and flushed with hydrogen gas until the pressure reached  $< 1$  mbar, after which the evacuation is repeated. Hydrogen pressures of 2 bar in the top compartment ( $p_{\text{high},0}$ ) and 1 bar in the bottom compartment ( $p_{\text{low},0}$ ) were applied, resulting in an initial differential pressure of 1 bar across the membrane. Subsequently, pressure sensors (Ahlborn FD821412A) were used in both compartments to detect the rise in pressure within the bottom chamber ( $p_{\text{low}}(t)$ ) over the course of 24–48 hours (or until no differential pressure was left). With the known volume of the lower chamber  $V$ , membrane thickness  $\delta_m$  and exposed area  $A_m$ , the permeability  $P_{\text{H}_2}^{\text{m,dry}}$  is obtained from a linear fit.

$$\ln\left(\frac{p_{\text{high},0} - p_{\text{low},0}}{p_{\text{high},0} - p_{\text{low}}(t)}\right) = \frac{P_{\text{H}_2}^{\text{m,dry}} A_m R T}{\delta_m V} t \quad (2)$$

### Electrochemical testing

The  $25 \text{ cm}^2$  testing was carried out in the designated test cell of the AEMDirekt consortium; the drawings of cell are published *via* the AEMDirekt consortium and available from the authors upon reasonable request. Prior to electrochemical testing, a  $6.5 \text{ cm} \times 7.5 \text{ cm}$  segment was cut from the electrode coating and activated *ex situ* at  $60 \text{ }^\circ\text{C}$  in 1 M KOH three times; the first two times 20 minutes and finally overnight, as aligned in funded project AEMDirekt.

The electrodes were benchmarked in two cell configurations: (1) the base cell design of AEMDirekt, where the cathode is contacted by a plain 316L Siemens-Energy-internal porous transport layer in order to be able to attribute all observations specifically regarding hydrogen crossover to the catalyst layers themselves (rather than masking any trends by the use of gas-diffusion-type electrodes); and (2) a performance-improved cell design where a Siemens-Energy-internal carbon fleece is inserted between the cathode catalyst layer and the stainless steel porous transport layer. In both configurations, the same plain stainless steel porous transport layer is used as anode transport layer and catalyst at once (similar to previous literature<sup>29</sup>). The tests were carried out at ambient pressure (1 bara + 150 mbar) on a testrig with symmetric lye circuits at  $60 \text{ }^\circ\text{C}$  (Fig. S1). Each side contained a 6 L electrolyte tank (DRB 237 6L 4xG1/4", Thielmann), which simultaneously served as a gas separator. 1 M potassium hydroxide solution was, unless otherwise noted, fed into both electrode compartments of the electrolyser cell at  $150 \text{ mL min}^{-1}$ . The gas streams from



the outlets of the gas separators were cleaned from any lye/aerosol particles with inline water spray nozzles (220.004.1Y.AC.00.0, Lechler). Subsequently, the gas streams were dried by cooling to 6 °C dew point (EC S, M&C). Thereafter, the gas impurities H<sub>2</sub> in O<sub>2</sub> (as well as O<sub>2</sub> in H<sub>2</sub>) were measured with a thermal conductivity sensor (FTC300, Pro-Chem Analytik) and fuel cell (Oxitrans II, Pro-Chem Analytik), respectively. A VMP-300 potentiostat with 70 A booster (Biologic) served as power source for the experiment.

After mounting the cell, the lye circuits were heated to 70 °C unless otherwise noted. Thereafter, a series of conditioning steps was carried out according to protocol harmonised across the AEMDirekt consortium, starting with a staircase holding 250 seconds each of 0.01 A cm<sup>-2</sup>, then 0.1 A cm<sup>-2</sup> and subsequently 0.1 A cm<sup>-2</sup> steps up to 1 A cm<sup>-2</sup>, which was held for 1 hour. Next, to ensure the cell being at equilibrium at the starting current density of the following characterisation of 1 mA cm<sup>-2</sup>, a 30-minute preparation interval at 1 mA cm<sup>-2</sup> was applied between the conditioning phase and the subsequent polarisation curve; the polarisation curve was carried out according to the EU-harmonised polarisation curve for high-current-density electrolyzers (up to 2 A cm<sup>-2</sup>).<sup>47</sup>

Following the conditioning phase and polarisation curve, a crossover staircase profile was run, starting at the largest current density of 2 A cm<sup>-2</sup>, followed by step-wise reductions of the current density to 1.5, 1, 0.75, and 0.5 A cm<sup>-2</sup> with a hold duration of 4 hours each, and ultimately 0.25 A cm<sup>-2</sup> (12 hours) and 0.1 A cm<sup>-2</sup> (24 hours). The longer hold durations at lower current densities were required to attain equilibrated gas impurity levels owed to the accordingly lower gas evolution rates. The testrings were programmed to stop operation in case any values greater 4% H<sub>2</sub> in O<sub>2</sub> or greater 0.8% O<sub>2</sub> in H<sub>2</sub> were reached. At least two reproductions were carried out for all of the H<sub>2</sub> crossover staircase profile, while five independent tests were carried out recording polarisation curves of each electrode configuration.

### Zeta potential analysis

The zeta potential at the electrode–water interface was determined from the measurement of the streaming potential with an electrokinetic analyzer for solid materials (SurPASS 3, Anton Paar). The electrode materials were deposited onto carbon fleece substrates and disks with a diameter of 14 mm were punched and mounted in the cylindrical compartment of the instrument's sample holder. The permeation mode of streaming potential measurement was selected where the aqueous test solution is forced to flow through the porous sample by means of an applied pressure difference. A 1 mM KCl solution was used as the base electrolyte and pH was adjusted with 0.05 M potassium hydroxide and 0.05 M hydrochloric acid, respectively. For ensuring an equilibrated electrode–water interface, the samples were rinsed four times prior to a triplicate measurement of the streaming potential at each pH titration step. The zeta potential calculated from the measured streaming potential according to the classic Smoluchowski equation is labelled 'apparent' to account for the unknown contribution of electrode conductance.

### Solid density measurements

Density measurements were performed on a gas pycnometer (Ultrapyc 5000 Micro, Anton Paar) using nitrogen as analysis gas. For analysis, the samples were cut into pieces and transferred into the micro cell (4.5 cm<sup>3</sup>). For achieving most precise results, the measurements were performed in "sample chamber first" direction at a pressure of 1.31 bar (sample chamber is pressurized, followed by pressure equilibration into the reference chamber). The sample chamber was prepared by a gas flow through the cell for 1 min.

### Physisorption

The physisorption measurements were performed on gas adsorption analyzers (Nova 800, Anton Paar and Autosorb 6100, Anton Paar). For analysis, the electrodes and blank membrane samples were cut into pieces and transferred into calibrated 9 mm (outer diameter) measuring cells with a large bulb. To activate the sample and remove physically adsorbed material from the surface, the samples were heated to 100 °C and evacuated for 12 h at the degassing stations integrated into the gas analyzers (such moderate conditions were chosen to prevent irreversible changes of the polymer membrane at elevated temperatures). The sample weight was determined before and after activation. A filler rod was inserted into the measurement cell after sample activation for reducing the void volume during analysis. Each filler rod was also inserted during cell calibration. For preventing gas intercalation into the polymer membrane, the void volume of the measurement cell was not determined using helium but calculated from the sample's density and the inner volume of the calibrated measuring cells with filler rod. The physisorption measurements on the electrodes were carried out using nitrogen as adsorptive on the analysis stations of the Nova 800. Due to the small specific surface area of the membrane reference, physisorption measurements on the membrane were carried out using Krypton on the Autosorb 6100 (due to the low saturation pressure of krypton and small number of non-adsorbed gas molecules in the sample cell, it is significantly more sensitive than nitrogen and therefore commonly used for analysis of thin films and low surface area materials<sup>46</sup>). All physisorption analysis were conducted at 77.35 K using liquid nitrogen as a cryogen for cooling the sample. BET analysis was performed in a range from 0.05–0.3 relative pressure.

### Capillary flow porometry

For characterizing the through pores in the electrodes, the catalyst pastes were deposited onto carbon felt substrates and were characterized using a capillary flow porometer (Porometer 3G zH, Anton Paar). For analysis, disks with a diameter of 24 mm were prepared by punching. Porofil was used a wetting fluid. The blank carbon fleece was measured as a reference. The wet measurement was conducted before the dry measurement.

### Author contributions

O. S., N. M. and H. M. selected the material systems for the experiments; O. S. and N. M. designed the catalyst pastes and



electrode coatings; M. K. and D. L. built the electrolysis testing stations; O. S. and H. M. designed experimental protocols and primary data analysis; D. L. carried out the electrolysis tests; F. N. G. and F. W. assisted the investigations with contact angle measurements; O. S. and F. N. G. carried out the rheology measurements; A. Malt. assisted the preparations of electrode pastes and application of electrode coatings; S. W-R., T. L. and S. F. carried out the physisorption and porosity measurements; P. B. and A. Malj. provided the anion-exchange membrane; A. K. and G. S. designed and coordinated the funding projects AEMDirekt and AEMReady. All authors contributed to discussions of the results. We thank Ella Maru Studio for the illustrations.

## Conflicts of interest

There are no conflicts of interest to declare.

## Data availability

The presented data is available from the authors upon reasonable request. Supplementary information (SI) is available in the online version of the article. See DOI: <https://doi.org/10.1039/d6ey00083e>.

## Acknowledgements

The investigations were partly funded by the German Federal Ministry of Research, Technology, and Space (Bundesministerium für Forschung, Technologie und Raumfahrt, BMFTR, former BMBF) under the contract number AEMDirekt (FKZ:03HY130A); early initial tests were carried out under AEMready (FKZ:03SF0 613B). Both projects were part of the H<sub>2</sub>Giga-flagship initiative launched within the German National Hydrogen Strategy in 2020.<sup>48</sup> The authors thank Markus Bierling (Siemens Energy) for fruitful discussions during the manuscript revision and Ella Maru Studio for the inspiring illustrations.

## References

- H. A. Miller, K. Bouzek, J. Hnat, S. Loos, C. I. Bernäcker and T. Weißgärber, *et al.*, Green hydrogen from anion exchange membrane water electrolysis: a review of recent developments in critical materials and operating conditions, *Sustainable Energy Fuels*, 2020, **4**(5), 2114–2133.
- W. U. Mulk, A. R. A. Aziz, M. A. Ismael, A. A. Ghoto, S. A. Ali and M. Younas, *et al.*, Electrochemical hydrogen production through anion exchange membrane water electrolysis (AEMWE): Recent progress and associated challenges in hydrogen production, *Int. J. Hydrogen Energy*, 2024, **94**, 1174–1211.
- I. O. Baibars, H. Huang, Y. Xiao, S. Wang, Y. Nie and C. Jia, *et al.*, Efficient hydrogen evolution at Ni/CeO<sub>x</sub> interfaces in anion-exchange membrane water electrolyzers, *Energy Environ. Sci.*, 2025, **18**(12), 6248–6259.
- Z. Guo, F. Lai, B. Song, S. Wang, H. Singh and P. Talebi, *et al.*, Scalable synthesis of amorphous NiFe oxide hollow microspheres via glucose-mediated spray pyrolysis for industrial hydrogen production, *Energy Environ. Sci.*, 2025, **18**(18), 8549–8563.
- T. B. Ferriday, S. N. Sampathkumar, P. H. Middleton, M. L. Kolhe and J. van Herle, A Review of Membrane Electrode Assemblies for the Anion Exchange Membrane Water Electrolyser: Perspective on Activity and Stability, *Int. J. Energy Res.*, 2024, **2024**, 1.
- I. Rios Amador, R. T. Hannagan, A. Qiang, S. W. Lee, N. Thi Thu Tran and K. M. K. Yap, *et al.*, Diagnosing mechanisms to mitigate anion exchange ionomer degradation during impure water electrolysis, *Energy Environ. Sci.*, 2025, **18**, 10195–10204.
- N. Chen, S. Y. Paek, J. Y. Lee, J. H. Park, S. Y. Lee and Y. M. Lee, High-performance anion exchange membrane water electrolyzers with a current density of 7.68 A cm<sup>-2</sup> and a durability of 1000 hours, *Energy Environ. Sci.*, 2021, **14**(12), 6338–6348.
- A. Hodges, A. L. Hoang, G. Tsekouras, K. Wagner, C. Y. Lee and G. F. Swiegers, *et al.*, A high-performance capillary-fed electrolysis cell promises more cost-competitive renewable hydrogen, *Nat. Commun.*, 2022, **13**(1), 1304.
- M. Moreno-González, P. Mardle, S. Zhu, B. Gholamkhash, S. Jones and N. Chen, *et al.*, One year operation of an anion exchange membrane water electrolyzer utilizing Aemion+ membrane: Minimal degradation, low H<sub>2</sub> crossover and high efficiency, *J. Power Sources Adv.*, 2023, **19**, 100109.
- R. Yanagi, P. Yang, A. W. Tricker, Y. Chen, M. C. Scott and S. A. Berlinger, *et al.*, Enhancing water and oxygen transport through electrode engineering for AEM water electrolyzers, *Joule*, 2025, **9**(7), 102001.
- M. M. Ikhsan, C. Yang, K. Ghotia, F. Egert, S. A. Ansar and O. Zurowska, *et al.*, Sulfonated polybenzimidazole for low-alkalinity ion solvating membrane water electrolysis, *Nat. Energy*, 2025, **10**, 1347–1359.
- R. Lira Garcia Barros, J. T. Kraakman, C. Sebregts, J. van der Schaaf and M. T. de Groot, Impact of an electrode-diaphragm gap on diffusive hydrogen crossover in alkaline water electrolysis, *Int. J. Hydrogen Energy*, 2024, **49**, 886–896.
- J. Witte, P. Trinke, B. Bensmann, M. Becker, R. Hanke-Rauschenbach and T. Turek, Influence of Contact Pressure on Hydrogen Crossover and Polarization Behavior in AEM Water Electrolysis, *J. Electrochem. Soc.*, 2025, **172**(1), 014502.
- P. Trinke, P. Haug, J. Brauns, B. Bensmann, R. Hanke-Rauschenbach and T. Turek, Hydrogen Crossover in PEM and Alkaline Water Electrolysis: Mechanisms, Direct Comparison and Mitigation Strategies, *J. Electrochem. Soc.*, 2018, **165**(7), F502.
- X. R. Wang, Y. Ma, J. Gao, T. Li, G. Z. Jiang and Z. Y. Sun, Review on water management methods for proton exchange membrane fuel cells, *Int. J. Hydrogen Energy*, 2021, **46**(22), 12206–12229.
- P. Berg, K. Promislow, J. St Pierre, J. Stumper and B. Wetton, Water Management in PEM Fuel Cells, *J. Electrochem. Soc.*, 2004, **151**(3), A341.



- 17 Y. Wu, H. Rabiee, X. S. Zhao, G. Wang and Y. Jiang, Insights into electrolyte flooding in flexible gas diffusion electrodes for CO<sub>2</sub> electrolysis: from mechanisms to effective mitigation strategies, *J. Mater. Chem. A*, 2024, **12**(24), 14206–14228.
- 18 J. Wu, G. Zhang, B. Dong, Y. Chang and Y. Chen, Experimental and simulation study of H<sub>2</sub> crossover in PEM water electrolysis for high-pressure hydrogen production up to 20 MPa, *Int. J. Hydrogen Energy*, 2025, **135**, 499–506.
- 19 O. Teschke, P. S. Casagrande, D. M. Soares and W. E. Gomes, Nanosized Water Channels Associated with Hydrophobic and Hydrophilic Fibrillar Arrangements Formed on Nafion Surfaces in Confined Regions, *ACS Omega*, 2024, **9**(22), 23567–23572.
- 20 D. Henkensmeier, M. Najibah, C. Harms, J. Žitka, J. Hnát and K. Bouzek, Overview: State-of-the Art Commercial Membranes for Anion Exchange Membrane Water Electrolysis, *J. Electrochem. Energy Convers. Storage*, 2021, **18**, 2.
- 21 S. Favero, I. E. L. Stephens and M. M. Titirci, Anion Exchange Ionomers: Design Considerations and Recent Advances - An Electrochemical Perspective, *Adv. Mater.*, 2024, **36**(8), e2308238.
- 22 C. Brussieux, P. Viers, H. Roustan and M. Rakib, Controlled electrochemical gas bubble release from electrodes entirely and partially covered with hydrophobic materials, *Electrochim. Acta*, 2011, **56**(20), 7194–7201.
- 23 T. Kadyk, D. Bruce and M. Eikerling, How to Enhance Gas Removal from Porous Electrodes?, *Sci. Rep.*, 2016, **6**, 38780.
- 24 R. Iwata, L. Zhang, K. L. Wilke, S. Gong, M. He and B. M. Gallant, *et al.*, Bubble growth and departure modes on wettable/non-wettable porous foams in alkaline water splitting, *Joule*, 2021, **5**(4), 887–900.
- 25 N. Yang, H. Li, X. Lin, S. Georgiadou, L. Hong and Z. Wang, *et al.*, Catalytic electrode comprising a gas diffusion layer and bubble-involved mass transfer in anion exchange membrane water electrolysis: A critical review and perspectives, *J. Energy Chem.*, 2025, **105**, 669–701.
- 26 M. A. Riaz, P. Trogadas, D. Aymé-Perrot, C. Sachs, N. Dubouis and H. Girault, *et al.*, Water electrolysis technologies: the importance of new cell designs and fundamental modelling to guide industrial-scale development, *Energy Environ. Sci.*, 2025, **18**(11), 5190–5214.
- 27 Federal Institute for Occupational Safety and Health. BACKGROUND DOCUMENT - Per- and polyfluoroalkyl substances (PFASs). 2025. Available from: <https://echa.europa.eu/hot-topics/perfluoroalkyl-chemicals-pfas>.
- 28 P. Jülich. Verbundvorhaben AEM-Direkt: Direktbeschichtung von anionenleitenden Membranen für großskalige Wasserelektrolyseure; Teilvorhaben: Stackdesign & elektrochemische Charakterisierung. Available from: <https://www.enargus.de/pub/bscw.cgi/26?op=enargus.eps2m=0v=10p=0q=Aem-direkt>.
- 29 B. Chen, A. L. G. Biancolli, C. L. Radford and S. Holdcroft, Stainless Steel Felt as a Combined OER Electrocatalyst/Porous Transport Layer for Investigating Anion-Exchange Membranes in Water Electrolysis, *ACS Energy Lett.*, 2023, **8**(6), 2661–2667.
- 30 H. Ito, N. Miyazaki, S. Sugiyama, M. Ishida, Y. Nakamura and S. Iwasaki, *et al.*, Investigations on electrode configurations for anion exchange membrane electrolysis, *J. Appl. Electrochem.*, 2018, **48**(3), 305–316.
- 31 A. W. Tricker, J. K. Lee, J. R. Shin, N. Danilovic, A. Z. Weber and X. Peng, Design and operating principles for high-performing anion exchange membrane water electrolyzers, *J. Power Sources*, 2023, **567**, 232967.
- 32 S. Koch, J. Disch, S. K. Kilian, Y. Han, L. Metzler and A. Tengattini, *et al.*, Water management in anion-exchange membrane water electrolyzers under dry cathode operation, *RSC Adv.*, 2022, **12**, 20778–20784.
- 33 K. Kiran, E. Bumenn, H. Kungl, E. Jodat, A. Karl and R. A. Eichel, Assessment of Dry Cathode Configuration in Anion Exchange Membrane Water Electrolysis: A Mini Review, *Electrochem. Sci. Adv.*, 2026, **6**, 1.
- 34 L. Gómez-Coma, Y. Gendel, P. M. Biesheuvel and S. Porada, Properties of Anion Exchange Membranes with a Focus on Water Electrolysis, *Membranes*, 2022, **12**(10), 989. Available from: <https://www.mdpi.com/2077-0375/12/10/989>.
- 35 A. Klinger, O. Strobl, H. Michaels, M. Kress, N. Martic and A. Maltenberger, *et al.*, Transport of Hydrogen Through Anion Exchange Membranes in Water Electrolysis, *Adv. Mater. Interfaces*, 2025, **12**, 5.
- 36 E. López-Fernández, C. G. Sacedón, J. Gil-Rostra, F. Yubero, A. R. González-Elipe and A. de Lucas-Consuegra, Recent Advances in Alkaline Exchange Membrane Water Electrolysis and Electrode Manufacturing, *Molecules*, 2021, **26**, 21.
- 37 S. Koch, L. Metzler, S. K. Kilian, P. A. Heizmann, F. Lombeck and M. Breitwieser, *et al.*, Toward Scalable Production: Catalyst-Coated Membranes (CCMs) for Anion-Exchange Membrane Water Electrolysis via Direct Bar Coating, *Adv. Sustainable Syst.*, 2023, **7**, 2.
- 38 G. Pätzold, M. Maier, L. Löttert, A. T. S. Freiberg, S. Thiele and D. Dworschak, Graded Roll-to-Roll Slot Die Coating for High-Throughput Catalyst Layer Studies, *ChemElectroChem*, 2025, **12**, 10.
- 39 Y. S. Zhang, N. E. Courtier, Z. Zhang, K. Liu, J. J. Bailey and A. M. Boyce, *et al.*, A Review of Lithium-Ion Battery Electrode Drying: Mechanisms and Metrology, *Adv. Energy Mater.*, 2022, **12**, 2.
- 40 C. D. Reynolds, P. R. Slater, S. D. Hare, M. J. H. Simmons and E. Kendrick, A review of metrology in lithium-ion electrode coating processes, *Mater. Des.*, 2021, **209**, 109971.
- 41 Y. Ma, C. Liu, M. Zhang and Y. Mai, Review on the effects of solvent physical properties on the performance of slot-die coated perovskite solar cells, *Surface Sci. Technol.*, 2024, **2**, 1.
- 42 C. D. Reynolds, S. D. Hare, P. R. Slater, M. J. H. Simmons and E. Kendrick, Rheology and Structure of Lithium-Ion Battery Electrode Slurries, *Energy Technol.*, 2022, **10**, 10.
- 43 T. Susanne, K. Wolfgang and L. Thomas, Zeta Potential of Photochemically Modified Polymer Surfaces, In *Progress in Colloid Polymer Science 132*, Springer Berlin Heidelberg, Berlin, Heidelberg, 2006, p. 54–61.
- 44 S. Rezaei Gomari, F. Amrouche, R. G. Santos, H. C. Greenwell and P. Cubillas, A New Framework to Quantify the Wetting Behaviour of Carbonate Rock Surfaces Based on



- the Relationship between Zeta Potential and Contact Angle, *Energies*, 2020, 13(4), 993.
- 45 R. Zimmermann, U. Freudenberg, R. Schweiß, D. Küttner and C. Werner, Hydroxide and hydronium ion adsorption – A survey, *Curr. Opin. Colloid Interface Sci.*, 2010, 15(3), 196–202, Available from: <https://www.sciencedirect.com/science/article/pii/S1359029410000038>.
- 46 M. Thommes, K. Kaneko, A. V. Neimark, J. P. Olivier, F. Rodriguez-Reinoso and J. Rouquerol, *et al.*, Physisorption of gases, with special reference to the evaluation of surface area and pore size distribution (IUPAC Technical Report), *Pure Appl. Chem.*, 2015, 87(9–10), 1051–1069.
- 47 T. Malkow, A. Pilenga, G. Tsotridis and G. de Marco, *EU Harmonised Polarisation Curve Test Method for Low Temperature Water Electrolysis*. 2018. Available from: <https://ec.europa.eu/jrc>.
- 48 Die Bundesregierung. Die Nationale Wasserstoffstrategie. Available from: [https://www.bundeswirtschaftsministerium.de/Redaktion/DE/Publikationen/Energie/die-nationale-wasserstoffstrategie.pdf?\\_\\_blob=publicationFile](https://www.bundeswirtschaftsministerium.de/Redaktion/DE/Publikationen/Energie/die-nationale-wasserstoffstrategie.pdf?__blob=publicationFile).

